

The Role of the Dopant in the Electronic Structure of Erbium-Doped TiO₂ for Quantum Emitters

J. B. Martins,¹ G. Grant,^{2, a)} D. Haskel,¹ G. E. Sterbinsky,¹ I. Masiulionis,^{2, a)} K. Sautter,^{2, a)} E. Karapetrova,¹ S. Guha,^{2, a)} and J. W. Freeland¹

¹⁾*X-ray Science Division, Argonne National Laboratory, Lemont, Illinois 60439, USA*

²⁾*Pritzker School of Molecular Engineering, University of Chicago, Chicago, Illinois 60637, USA*

(*Electronic mail: jbarbosamartins@anl.gov)

(Dated: 1 October 2024)

Erbium-doped TiO₂ materials are promising candidates for advancing quantum technologies, necessitating a thorough understanding of their electronic and crystal structures to tailor their properties and enhance coherence times. This study explored epitaxial erbium-doped rutile TiO₂ films deposited on r-sapphire substrates using molecular beam epitaxy. Photoluminescence excitation spectroscopy demonstrated decreasing fluorescence lifetimes with erbium doping, indicating limited coherence times. Lattice distortions associated with Er³⁺ were probed by X-ray absorption spectroscopy, indicating that erbium primarily occupies Ti⁴⁺ sites and influences oxygen vacancies. Significant lattice distortions in the higher-order shells and full coordination around erbium suggest that additional defects are likely prevalent in these regions. These findings indicate that defects contribute to limited coherence times by introducing alternative decay pathways, leading to shorter fluorescence lifetimes.

I. INTRODUCTION

The relentless growth in data storage and the continuous trend of device miniaturization has driven technological progress to approach the quantum limit.^{1,2} Quantum Information Science (QIS), grounded in the principles of quantum mechanics, emerges as a groundbreaking solution for efficient data handling, secure information exchange, and long-distance communication while ensuring data integrity.^{3,4} At the heart of quantum technologies lies the manipulation of qubits, the fundamental units of quantum information.^{4,5} Quantum coherence plays a crucial role in realizing quantum technologies⁶, which enables qubits to maintain the superposition of quantum states. However, the challenge lies in preserving coherence which is limited by the inherent susceptibility to environmental influences. Therefore, ensuring the prolonged persistence of quantum states in superposition (i.e., long coherence time) is essential for successfully implementing quantum information technologies.^{5,6}

Solid-state spin qubits show significant promise among the candidates for QIS applications, owing to their compatibility with conventional microelectronics.^{5,6} Nevertheless, the properties of solid-state spin qubits are linked to their crystal host, necessitating material engineering to enhance the quantum emitter's properties and mitigate decoherence sources like charge carriers or phonons. Among potential candidates, rare-earth ions (REIs) in solid-state systems stand out.⁷ Specifically, the trivalent erbium ion (Er³⁺) is noteworthy for its optical 4f–4f transition within telecom-C band, aligning with the low-loss transmission in optical fibers, making it an ideal quantum emitter for quantum network systems.^{8–13} Selecting the optimal crystal host for REIs in QIS involves consider-

ing factors such as low nuclear and electron spin concentrations, nonpolar symmetry, and a large band gap.^{6,13,14} These factors are instrumental in not only enhancing optical transitions but also in mitigating local effects in the vicinity of REIs, thereby addressing coherence issues effectively. Previous studies identified TiO₂ as a promising host for Er³⁺, with the rutile and anatase phases being particularly stable.^{15,16} Recent research on Er-doped TiO₂ films and bulk crystals has demonstrated narrow optical inhomogeneous linewidths, underscoring the importance of buffer and capping layers in enhancing optical properties.^{15,17} Despite these advancements, further understanding is needed on how Er³⁺ dopants influence the TiO₂ host lattice's electronic and crystal structure.

This investigation focuses on epitaxial erbium-doped rutile TiO₂ thin films grown on *r*-plane sapphire substrates, aiming to explore how erbium incorporation affects the material's coherence times. We employed spectroscopy and diffraction techniques to correlate structural modifications with variations in coherence times. The selection of sapphire as the substrate was deliberate, as it enables the formation of high-quality single-crystal rutile TiO₂. X-ray diffraction (XRD) confirmed the persistence of single crystallinity despite doping. Variations on the Er³⁺ fluorescence lifetimes, which set the upper bounds for coherence times, were assessed using photoluminescence excitation (PLE) spectroscopy revealing a downward trend with increasing doping. Additionally, information on local coordination, lattice distortion, and chemical environment near erbium sites was probed using X-ray absorption spectroscopy (XAS) and extended X-ray absorption fine structure (EXAFS). The analyses indicate that doping increases oxygen vacancy defect density within TiO₂. Furthermore, they suggest that erbium ions are fully coordinated, indicating redistribution of oxygen vacancies away from the Er sites. This increase in additional defect density is likely to limit coherence by introducing alternative decay pathways upon Er³⁺ excitation.

^{a)}Also at Materials Science Division, Argonne National Laboratory, Lemont, Illinois 60439, USA

II. METHODS

A. Samples Growth

Epitaxial Er:TiO₂ thin films were deposited using a Riber C21 DZ Cluster molecular beam epitaxy (MBE) system. Titanium tetraisopropoxide (TTIP) from Sigma-Aldrich with a purity of 99.999% (trace metal basis) was the titanium precursor as in the TTIP-based MBE of TiO₂ detailed elsewhere.¹⁸ Growths were carried out on a r-plane (102) sapphire substrate at 640 °C temperature, oxygen partial pressure of 7×10^{-6} torr, and a TTIP beam-equivalent flux of 3.5×10^{-6} . The growth rate was 32.5 nm per hour. *In-situ* erbium (Er) doping (20, 200, and 500 ppm) using metallic Er was carried out by a high-temperature (860 °C to 990 °C) effusion cell.

B. Structural and optical characterization

Single crystal X-ray diffraction characterization was carried out at the 33BM beamline of the Advanced Photon Source (APS) at a photon energy of 20 keV. PLE spectroscopy was performed in a custom confocal microscopy setup designed for telecom C-band measurement of thin films, with samples mounted in a cryostat at 3.5 K (s50 Cryostation, Montana Instruments). A tunable 1.5 μ m laser illuminated the samples for 1.5 ms using pulses shaped by acousto-optic modulators. Emission from the samples subsequent to excitation was then collected by a Quantum Opus superconducting nanowire single photon detector (SNSPD) for 3 ms collection intervals. Sweeping the excitation laser wavelength resulted in PLE spectrum and excited state lifetime measurements at each wavelength for each measured sample. Additional information on this experimental setup is given in detail elsewhere¹². XAS measurements were conducted at O *K*-edge, Ti *L*-edge, and Er *M*₅-edges at the 29ID beamline at the Advanced Photon Source (APS). The beam was directed along surface normal, and the spectra were averaged over the acquired horizontal and vertical polarization to ensure orientation-independent assessment of the local environment. The EXAFS measurements were performed at the 20-BM beamline of the APS. Data collection was conducted in a grazing incidence geometry, with an angle of incidence of a few degrees and with linear x-ray polarization in the plane of the film. The sample was rotated about the film surface normal to average in-plane polarizations. The temperature was maintained at 300 K throughout the entire experiment. Since the [101] direction is along the surface normal, separate FEFF8 simulations were carried out with linear polarization along orthogonal in-plane [-101] and [010] directions to obtain theoretical phase shifts and scattering amplitudes¹⁹.

III. RESULTS AND DISCUSSION

A. Characterization of epitaxial Er:TiO₂ films by single crystal X-ray diffraction

Figure 1 shows the single crystal X-ray diffraction spectra, confirming the (012)_{Al₂O₃} direction normal to the r-plane surface through the specular (0, K, 2K) scan. The film shows a main peak of (101)_{TiO₂} film orientation on the r-plane surface consistent with previous literature^{20,21}. Position of the peaks are roughly equivalent with the expected bulk values indicating that the films are relaxed. The lattice parameter approximates that of bulk TiO₂. As was noted in previous work²⁰, the matching of the symmetry between the (012)_{Al₂O₃} and (101)_{TiO₂} planes, leads to a twinned structure with alternating domains on 10's of nm lengthscales. These domains likely lead to a relaxation to the bulk lattice values due to the high-density of domain walls. Additionally, all films exhibit a minority (301) orientation, which may result from the high density of twin domains. No systematic behavior with doping was observed, suggesting that the minority (301) orientation is unrelated to doping.

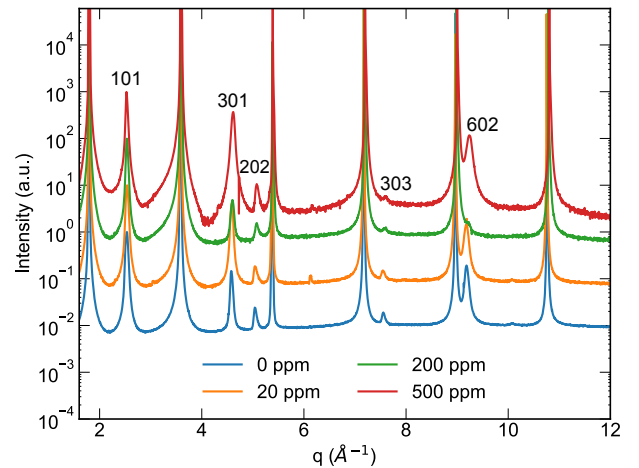


FIG. 1: (101) Rutile TiO₂ grown on the (012) surface of sapphire, exhibiting primary (101) orientation with a minor (< 10%) phase with a (301) orientation.

B. Impact of erbium concentration on optical properties

The impact of increasing Er³⁺ dopant density on the rutile TiO₂ host lattice was investigated by optical characterization of the thin film samples performed via time-resolved PLE spectroscopy. Figure 2a shows the resulting absorption spectra near 1.5 μ m resonance for the series of single crystal erbium-doped rutile TiO₂ films. The ground (⁴I_{15/2}) and excited (⁴I_{13/2}) electronic states of Er³⁺ in rutile split into eight (Z₁₋₈) and seven (Y₁₋₇) Kramers' doublets, respectively (Figure 2b)¹⁵ with D_{2h} point symmetry for Er³⁺ occupying Ti⁴⁺ sites in rutile TiO₂. The growing background towards

the lower wavelengths (i.e., higher energies) stems from off-resonant absorption.

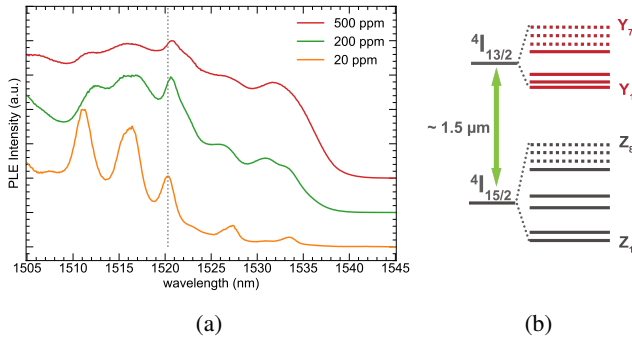


FIG. 2: (a) PLE spectra for the set of Er-doped TiO₂ thin films. (b) Energy level diagram for $^4I_{15/2} \rightarrow ^4I_{13/2}$ transition in Er³⁺ ion.

We focus our discussion on the peak highlighted by a vertical dashed line (approximately 1520 nm), which corresponds to the Er³⁺ Z₁ → Y₁ transition in rutile-phase TiO₂.¹⁵ The narrowest observed inhomogeneous linewidth of approximately 50 GHz is found in the sample doped with 20 ppm erbium and increases with higher dopant concentrations. The broadening of the linewidth can be attributed to electric fields generated by charged defects near the Er³⁺ sites, including negatively charged point defects resulting from Er³⁺ substituting Ti⁴⁺ sites (i.e., the negative charge upon replacement of Ti⁴⁺ to Er³⁺), and positively charged oxygen vacancy point defects.^{17,22–25}

The fluorescence lifetimes at the highlighted peak (Table I) exhibit a dopant-driven decreasing trend. This shortening of lifetime is consistent with prior observations in CeO₂ with increasing erbium doping, where the decrease is attributed to the introduction of defects. While the exact nature of these defects remains uncertain, they likely introduce non-radiative or quenching pathways that shorten the fluorescence lifetimes²⁶. If the defects were strictly localized to individual Er sites, their interaction would be limited, and neither significant linewidth broadening nor a pronounced reduction in lifetime would be expected. However, the increased linewidth and shorter fluorescence lifetimes at higher dopant concentrations suggest that the defects surrounding the Er³⁺ sites are not confined to the immediate vicinity but instead form more extended distributions. These extended defects likely modify the local crystal field around the Er ions, thereby influencing the observed optical properties.

The lifetime of the excited state sets an upper limit for the coherence time. Thus, a shorter fluorescence lifetime indicates a more rapid decay of the excited state, which impacts the persistence of quantum superposition and, in consequence, coherence time of the quantum system. Therefore, the observed dopant-driven decrease in the excited state lifetime is critical in assessing the material's coherence times. Understanding the nuances of local electronic and crystal structures is pivotal for comprehending the alterations in the inherent op-

TABLE I: Er³⁺ fluorescence lifetimes for Er-doped rutile TiO₂ samples.

Er Concentration (ppm)	Lifetime (ms)
20	2.1 (3)
200	0.99 (2)
500	0.63 (1)

tical properties of Er-doped rutile TiO₂ with varying erbium concentrations.

C. Influence of erbium on the electronic structure of TiO₂ host lattice

To further elucidate these modifications, we employed XAS to investigate erbium-induced changes in the local electronic structure within the crystal lattice. Starting with oxygen spectroscopy, the O *K*-edge spectra displayed in Figure 3a are a result of electronic transitions from O(*1s*) states to unoccupied O(*2p*) states. The spectra were acquired in both total electron yield (TEY) and fluorescence yield (FY) modes, represented by solid and dashed lines respectively. The primary distinction between TEY and FY acquisition modes lies in their depth sensitivity, with TEY being more surface-sensitive and FY more bulk-sensitive. In terms of symmetry, TiO₂ consists of a central Ti⁴⁺ surrounded by six O²⁻ ions and the octahedral crystal field splits the Ti(*3d*) orbitals into *t*_{2g} and *e*_g states^{27–29}. Geometrically, the *e*_g orbitals from Ti point toward the O *2p* orbitals, while the *t*_{2g} lobes point between the O atoms leading to strong hybridization between O(*2p*) and Ti(*3d*) orbitals. The significant hybridization leads to two distinguishable pre-peaks at approximately 530 eV and 533 eV labeled as *t*_{2g} and *e*_g respectively. Moreover, three distinct features at higher energies, with peaks around 539 eV, 542 eV, and 545 eV, denoted as C, D, and E, correspond to delocalized O(*2p*)–Ti(*4s*) and O(*2p*)–Ti(*3d*) hybridized states and are a fingerprint of the rutile phase in TiO₂.³⁰

Two notable trends emerge from comparing the TEY and FY spectra. Firstly, the intensity ratio of the *t*_{2g} and *e*_g pre-peaks varies with increasing erbium concentration in both TEY and FY spectra, suggesting that these variations are not confined to the surface and exist in the bulk of the film as well. Secondly, the FY spectra, which provide greater depth sensitivity than TEY, display broader peaks between 538 and 545 eV. This broadening is attributed to contributions from the sapphire substrate³¹. Due to the strong hybridization between O(*2p*) and Ti(*3d*) orbitals, the *t*_{2g} and *e*_g pre-peaks in the O *K*-edge spectra are expected to be highly sensitive to changes in the electronic structure. Thus, the fitting analysis illustrated in Figure 3b focused on the two pre-peaks in the TEY spectra to gain insights into the electronic structure of the host lattice. Gaussian functions were fitted to the spectra, revealing two distinct features labeled as A* and B*, adjacent to the main *t*_{2g} and *e*_g peaks, respectively. These adjacent features are approximately 1 eV blue-shifted from the main peaks and can be attributed to modifications in the electronic structure of the

TABLE II: Peak areas obtained from the Gaussian fitting analysis of pre-peaks in XANES O *K*-edge spectra. Two main trends are observed. First, the overall decrease in areas of the main t_{2g} and e_g pre-peaks with increasing erbium concentration. In contrast, erbium-driven increasing in the A^* and of B^* areas suggest generation of oxygen vacancies within the host lattice.

Er Concentration (ppm)	Peak Area (a.u.)			
	t_{2g}	A^*	e_g	B^*
0	1.22 (14)	0.47 (9)	1.13 (8)	0.24 (7)
20	0.86 (14)	0.76 (9)	0.98 (8)	0.33 (7)
200	0.77 (14)	0.73 (9)	0.84 (8)	0.40 (7)

rutile lattice related to oxygen vacancies³².

Notably, the A^* and B^* features are present even in the undoped sample, indicating non-stoichiometric TiO₂. Their area increases with erbium doping, as detailed in Table II. Native point defects, such as neutral or charged oxygen vacancies, are common in wide-bandgap metal oxides like TiO₂^{33,34}. The increase in A^* and B^* areas with doping suggests that erbium introduces new oxygen vacancies into the lattice. Each Er ion is expected to create only half an oxygen vacancy to balance the charge (i.e., one O_v²⁺ vacancy balances the charge of two Er³⁺ ions). Despite this, the substantial increase in A^* and B^* peak areas implies that defects around different Er sites likely overlap or interact. This overlap leads to significant changes in the XAS spectra, even at low Er concentrations, suggesting that the defects are likely not isolated but form a more extensive network within the material. Moreover, the erbium-driven increase in A^* and B^* areas is accompanied by a decrease in the t_{2g} and e_g peak areas, reflecting disruptions in the local electronic structure. The creation of new oxygen vacancies disrupts the strong hybridization between O($2p$) and Ti($3d$) orbitals, leading to reduced overlap and thus smaller t_{2g} and e_g peak areas.

Similarly to the O *K*-edge, the Ti *L*-edge XAS spectra are sensitive to changes in electronic structure due to the hybridization of O($2p$) and Ti($3d$) orbitals. Therefore, the Ti *L*-edge was probed using TEY mode to investigate possible dopant-induced modifications in the electronic structure (Figure 4). The fine structure in the L_3 and L_2 edges results from the breaking of degenerate electronic orbitals by the lattice crystal field, leading to the splitting of $3d$ states into three-fold t_{2g} and two-fold degenerate e_g states. Further distortion from the octahedral lattice induces additional splitting, particularly evident at the L_3 -edge. The first two weak pre-edge peaks are associated with combined effects of particle-hole coupling and crystal field splitting^{35,36}. These features exhibit low intensity due to the incomplete screening of the core hole and the influence of multiplet effects, which reduce the transition intensity. The intense, narrow peak around 458 eV corresponds to the t_{2g} state, while the split e_g states produce two peaks associated with the TiO₂ crystal phase.

Expected consequences of doping include charge compensation through the formation of additional defects, such as oxygen vacancies and Ti³⁺, as well as distortions of the host

lattice.^{25,37,38} Prior investigations on Cr-doped rutile TiO₂ highlighted the critical role of oxygen point defects in stabilizing Cr³⁺ ions, particularly through the formation of complex defects involving two Cr atoms and one oxygen vacancy³⁸. This stabilization is associated with distortions in the crystal lattice due to the elongation of Ti–O bonds, which affect the Ti e_g orbitals. These orbitals are highly sensitive to changes in the local environment because they interact directly with the $2p$ orbitals of the surrounding O atoms. As the local symmetry and crystal field around the Ti ions change, the energy levels of the e_g orbitals shift accordingly. In our study, the low concentration of Er³⁺ dopant—on the order of hundreds of parts per million (ppm)—makes it challenging to observe significant lattice distortions or prominent features associated with e_g orbital splitting or Ti³⁺-related signals. However, comparisons between undoped and doped samples reveal an overall decrease in spectral intensity with Er doping, suggesting that the dopant induces changes in the local electronic environment around the Ti ions. These changes may arise from slight distortions in the Ti–O coordination environment, which in turn alter the crystal field and electronic structure of the Ti sites.

To gain deeper insight into how the dopant affects the formation of additional defects within the host lattice Erbium spectroscopy was performed. The XAS spectrum at the Er M_5 -edge (Figure 5) exhibits three distinct peaks corresponding to $3d \rightarrow 4f$ transitions. These transitions, characterized by changes in the total angular momentum quantum number ($\Delta J = 0, \pm 1$), are indicative of erbium in the trivalent state³⁹.

D. Structural distortions upon erbium incorporation into TiO₂

The local environment around the Er³⁺ sites was further examined using EXAFS at the Er *L*-edge and Ti *K*-edge as depicted in Figure 6. A comparison of the experimental data with FEFF simulations is shown in Figures 6a and 6d, where the Fourier-transformed (FT) XAFS data for the Ti *K*-edge and Er L_3 -edge, respectively, are represented by solid lines.

These comparisons revealed significant differences, particularly in the FT Er L_3 -edge spectra, where a marked shift towards higher distances in the first shell was observed, along with a notable suppression in the higher-R structure. These observations suggest alterations in the local structure around erbium, such as bond length variations or changes in coordination numbers at greater distances. The experimental data, acquired at 300 K, were scaled by a factor of 2 in these two plots to better match with simulations conducted at 0 K.

Figures 6e and 6b display FT XAFS data and fits for Er L_3 -edge and Ti *K*-edge, respectively. Each polarization contribution was equally weighted (0.5) in the fits to account for in-plane polarization and sample spin, employed during the data acquisition to reduce Bragg peak artifacts in the experiment. The analysis involved simultaneous fitting of data weighted by different k -weights to minimize correlations between coordination number and the Debye-Waller factor (σ^2). The small nominal split of 0.04 Å in first shell Ti/Er–O distances can-

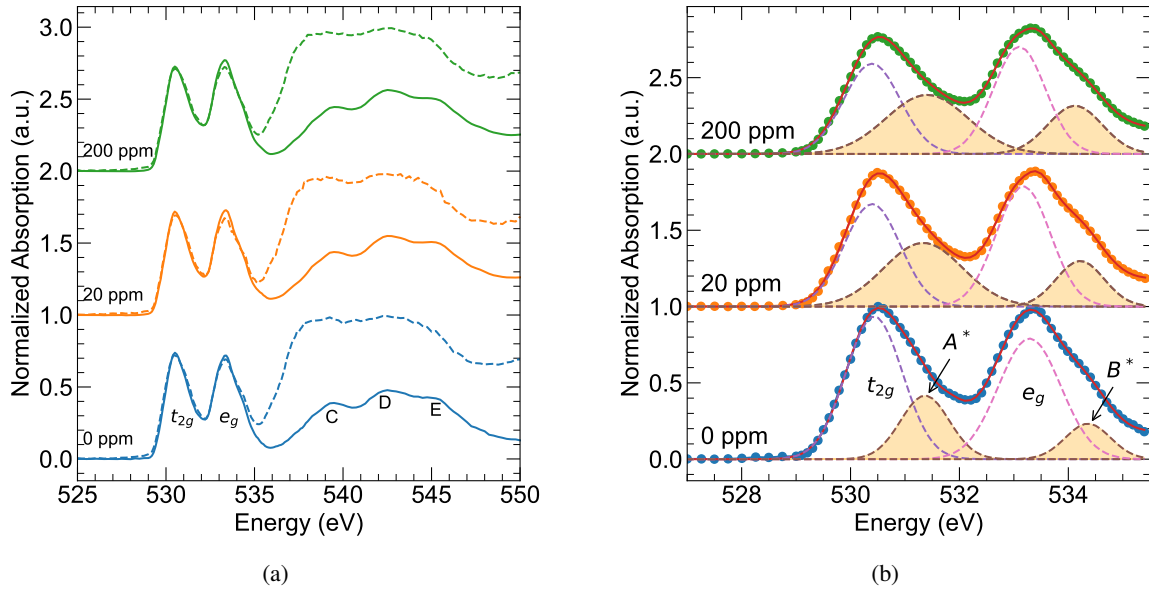


FIG. 3: (a) XAS O K -edge spectra for undoped (0 ppm) and Er-doped (20 and 200 ppm) TiO₂ films, measured via surface-sensitive TEY mode (solid lines) and bulk-sensitive FY mode (dashed lines). (b) Gaussian fit analysis of TEY spectra depicting pre-peaks A and B, corresponding to electron transitions from O 1s shell into unoccupied O 2p orbitals hybridized with Ti t_{2g} and e_g orbitals, respectively, with adjacent features A* and B* indicating oxygen vacancies.³²

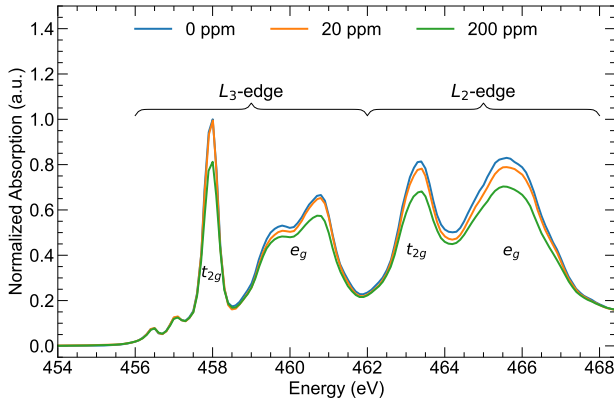


FIG. 4: Ti L-edge spectra for undoped (0 ppm) and Er-doped TiO₂ samples (20 ppm and 200 ppm).

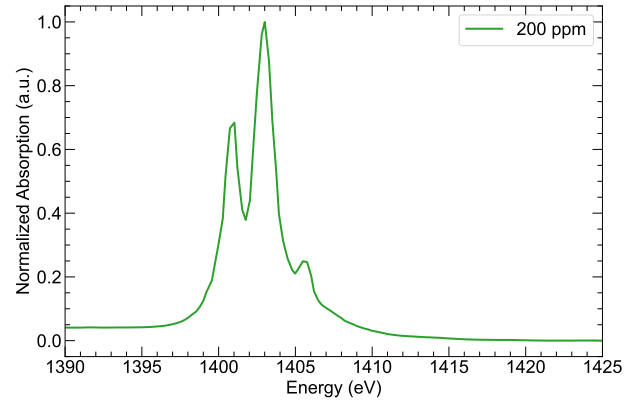


FIG. 5: XAS spectrum at the Er M_5 edge for 200 ppm doped Er:TiO₂.

not be resolved with the limited k -range of the XAFS data ($k_{\max} \sim 10 \text{ \AA}^{-1}$) hence the fitted bond length correction was forced to be proportional to the nominal bond lengths. Similarly, coordination numbers of split distances were fitted while maintaining their ratio fixed to nominal values. The FT Er L_3 -edge spectrum (Figure 6e) revealed erbium coordinated to oxygen for the first shell (Er–O), with an expanded bond length of 2.20 Å (Table III). This distance is significantly larger than the corresponding Ti–O₍₁₎ bond length of 1.92 Å observed in the Ti K -edge analysis, indicating a local expansion in the lattice around the erbium dopant. Additionally, the presence of Ti neighbors at a distance of 3.09 Å in the second shell suggests that Er³⁺ is occupying Ti⁴⁺ lattice sites.

The significant local expansion observed around Er

aligns with the difference in ionic radii between Er³⁺ and Ti⁴⁺. The theoretical difference in ionic radii is 0.29 Å (0.89 Å – 0.605 Å⁴⁰), which closely matches the experimental local expansion of 0.28 Å, as indicated by the difference between the Er–O₍₁₎ bond length (2.20 Å) and the Ti–O₍₁₎ bond length (1.92 Å) listed in Table III. This close agreement between theoretical and experimental values, combined with nominal (N=2) Er–Ti coordination in the second shell at a bond distance of 3.09 Å, supports the hypothesis that Er³⁺ is substituting at Ti⁴⁺ sites, albeit with significant lattice distortion especially at higher order shells. Interestingly, the amplitude of Ti K -edge XAFS is somewhat reduced in the doped sample, despite the rather low doping level of 500 ppm, indi-

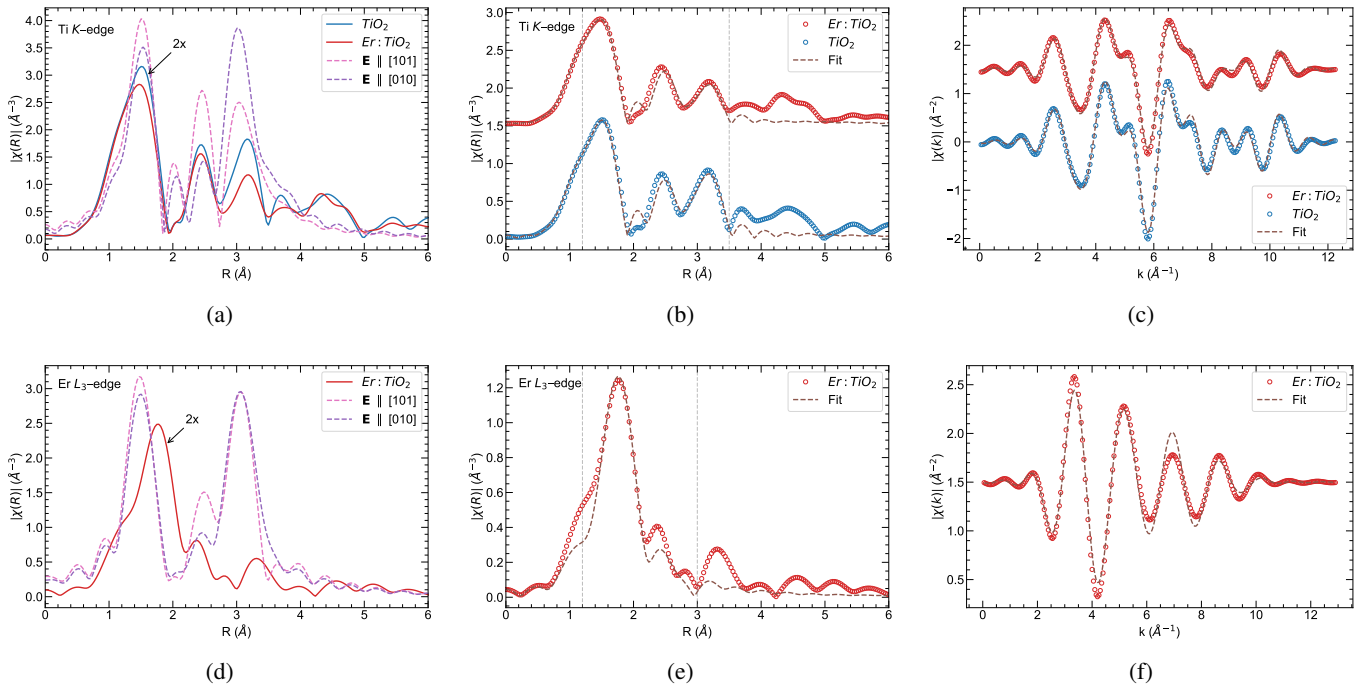


FIG. 6: Fourier-transformed (a) Ti K -edge and (d) Er L_3 -edge XAS spectra of undoped (solid blue) and 500 ppm Er-doped (solid red) TiO₂ samples. The k range used in the FTs was $[2-11] \text{ \AA}^{-1}$ and $[2-10] \text{ \AA}^{-1}$ for Ti K and Er L_3 -edges, respectively. The dashed curves represent FEFF simulations for electric field polarizations along the $[010]$ and $[-101]$ directions. Fitted Fourier-transformed (b) Ti K -edge and (c) Er L_3 -edge spectra for undoped (blue circles) and 500 ppm Er-doped TiO₂ (red circles) with vertical dashed lines showing the regions used in the real-space fits. Panels (c) and (f) show the back Fourier transform of data and fits in the real-space region marked by the vertical lines for the Ti K -edge and Er L_3 -edge, respectively

indicating that structural distortions around Er ions are extended, affecting a larger % of Ti ions. These results can also be correlated to the overall intensity decreasing in Ti L -edge XAS spectra with doping portrayed in Figure 4, as erbium ions appear to cause lattice distortions. The Ti K -edge analysis (Figure 6b) for the undoped sample (blue circles) yielded fitted distances closely resembling the nominal TiO₂ structure. Small differences were observed for the doped sample (red circles), although signatures of increased disorder are present particularly at the longer Ti-Ti correlations (Table III). The same amplitude reduction factor (S_0^2) of 0.93 was used for both the Ti K -edge and Er L_3 -edge fits to ensure consistency across the analyses.

The substitution of Ti⁴⁺ by Er³⁺ ions raises important questions about the mechanisms of charge compensation that stabilize the dopant within the host structure. The increased area of the A^* and B^* features in the O K -edge spectra, which are associated with oxygen vacancies, suggests that these vacancies play a key role in compensating for the charge imbalance introduced by Er³⁺ ions, thereby maintaining charge neutrality^{41,42}. EXAFS analysis indicates that the first coordination shell of both Er³⁺ and Ti⁴⁺ remains fully occupied by oxygen, as reflected by coordination numbers close to 6 for both species. Specifically, the coordination number of Er–O is 6.4 (3) (Table III), while the coordination number for Ti–O is 6.2 (3), supporting full occupation in the first shell. However, the error bars of around 5% in coordination number al-

low for the presence of oxygen vacancies in the first Ti–O shell. Thus, while the first shell appears fully occupied within experimental uncertainty, the possibility of oxygen vacancies beyond the first Er–O shell in the lattice cannot be ruled out.

The σ^2 factors indicate increased disorder beyond the first shell, particularly around the Er³⁺ ions, with a value of 0.0140 (5) \AA^2 for the Er–Ti₍₁₎ distance. Additionally, major differences between the data and simulations in the higher shells (Fig. 6d point to erbium-driven structural changes beyond the first coordination shell, which may include oxygen vacancies located farther from the Er³⁺ sites. We were unable to model the Er local structure beyond the Er–Ti₍₁₎ distance. The long-range distortions in the local environment around Er³⁺ ions, extending to at least 4 \AA , suggest that these defects are not isolated but cause widespread changes in the lattice. Even at 500 ppm doping levels these extensive distortions may overlap affecting a significant amount of Ti atoms, as suggested by the Ti K - and L -edge probes.

Finally, revisiting the PLE discussion, the observed decrease in fluorescence lifetime of Er³⁺ can be attributed to the dopant-induced generation of oxygen vacancies. These point defects act as non-radiative recombination centers, enabling energy transfer between Er³⁺ ions and oxygen vacancy defects, which leads to a quenching effect. Consequently, the fluorescence lifetime decreases due to enhanced non-radiative recombination pathways. Since the fluorescence lifetime imposes an upper limit on coherence time in quantum systems,

the observed reduction in fluorescence lifetimes indicates a corresponding decrease in coherence times.

In conclusion, our investigation into epitaxial Er-doped rutile TiO₂ thin films reveals significant effects of erbium doping on both structural and electronic properties. XAS analysis at the O *K*-edge indicates that erbium doping leads to the formation of oxygen vacancies, which alter the electronic structure of the host lattice. EXAFS analysis for the Er *L*₃-edge spectra indicates that Er³⁺ ions substitute for Ti⁴⁺ ions in the TiO₂ lattice. This substitution results in notable lattice distortions due to the larger ionic radius of Er³⁺ compared to Ti⁴⁺. Coordination number analysis reveals consistent six-fold coordination around erbium, suggesting that neighboring oxygen ions stabilize the local charge environment. However, while our findings indicate significant distortions in higher-order shells, which are likely associated with oxygen vacancies displaced from the first shell, further comparative studies are necessary to definitively determine the exact substitution sites. The broadening of the *f*–*f* excitation observed in PLE suggests a distribution of crystal fields, indicating structural disorder extending beyond the first coordination shell. This disorder impacts the crystal field sensed by the 4*f* electrons. The lattice distortions and additional point defects are expected to enhance non-radiative energy transfer, which correlates with the reduced fluorescence lifetimes observed by PLE. This underscores the complex interplay between dopant-induced structural modifications and optical properties, emphasizing the importance of detailed local electronic and crystal structure investigations for advancing quantum information processing technologies.

ACKNOWLEDGMENTS

This work was supported by Q-NEXT, a U.S. Department of Energy Office of Science National Quantum Information Science Research Centers under Award No. DE-FOA-0002253. The use of the Advanced Photon Source, Argonne National Laboratory was supported by the U.S. Department of Energy, Office of Science, Basic Energy Sciences, under Contract No. DE-AC02-06CH11357.

DATA AVAILABILITY STATEMENT

The data that support the findings of this study are available within the article.

- ¹D. D. Awschalom, R. Hanson, J. Wrachtrup, and B. B. Zhou, “Quantum technologies with optically interfaced solid-state spins,” *Nature Photonics* **12**, 516–527 (2018).
- ²A. Laucht, F. Hohls, N. Ubbelohde, M. F. Gonzalez-Zalba, D. J. Reilly, S. Stobbe, T. Schrder, P. Scarlino, J. V. Koski, A. Dzurak, C.-H. Yang, J. Yoneda, F. Kuemmeth, H. Bluhm, J. Pla, C. Hill, J. Salfi, A. Oiwa, J. T. Muhonen, E. Verhagen, M. D. LaHaye, H. H. Kim, A. W. Tsen, D. Culcer, A. Geresdi, J. A. Mol, V. Mohan, P. K. Jain, and J. Baugh, “Roadmap on quantum nanotechnologies,” *Nanotechnology* **32**, 162003 (2021), 2101.07882.
- ³A. Acín, I. Bloch, H. Buhrman, T. Calarco, C. Eichler, J. Eisert, D. Esteve, N. Gisin, S. J. Glaser, F. Jelezko, S. Kuhr, M. Lewenstein, M. F. Riedel,

- P. O. Schmidt, R. Thew, A. Wallraff, I. Walmsley, and F. K. Wilhelm, “The quantum technologies roadmap: a European community view,” *New Journal of Physics* **20**, 080201 (2018), 1712.03773.
- ⁴D. P. DiVincenzo, “Quantum Computation,” *Science* **270**, 255–261 (1995).
- ⁵G. Zhang, Y. Cheng, J.-P. Chou, and A. Gali, “Material platforms for defect qubits and single-photon emitters,” *Applied Physics Reviews* **7**, 031308 (2020).
- ⁶G. Wolfowicz, F. J. Heremans, C. P. Anderson, S. Kanai, H. Seo, A. Gali, G. Galli, and D. D. Awschalom, “Quantum guidelines for solid-state spin defects,” *Nature Reviews Materials* **6**, 906–925 (2021).
- ⁷T. Zhong and P. Goldner, “Emerging rare-earth doped material platforms for quantum nanophotonics,” *Nanophotonics* **8**, 2003–2015 (2019).
- ⁸T. Böttger, C. W. Thiel, R. L. Cone, and Y. Sun, “Effects of magnetic field orientation on optical decoherence in Er³⁺:Y₂SiO₅,” *Physical Review B* **79**, 115104 (2009).
- ⁹D. Serrano, S. K. Kuppasamy, B. Heinrich, O. Fuhr, D. Hunger, M. Ruben, and P. Goldner, “Ultra-narrow optical linewidths in rare-earth molecular crystals,” *Nature* **603**, 241–246 (2022), 2105.07081.
- ¹⁰A. M. Dibos, M. T. Solomon, S. E. Sullivan, M. K. Singh, K. E. Sautter, C. P. Horn, G. D. Grant, Y. Lin, J. Wen, F. J. Heremans, S. Guha, and D. D. Awschalom, “Purcell Enhancement of Erbium Ions in TiO₂ on Silicon Nanocavities,” *Nano Lett.* **22**, 6530–6536 (2022), 2204.09859.
- ¹¹M. Rancić, M. P. Hedges, R. L. Ahlefeldt, and M. J. Sellars, “Coherence time of over a second in a telecom-compatible quantum memory storage material,” *Nat. Phys.* **14**, 50–54 (2018), 1611.04315.
- ¹²C. Ji, M. T. Solomon, G. D. Grant, K. Tanaka, M. Hua, J. Wen, S. K. Seth, C. P. Horn, I. Masiulionis, M. K. Singh, S. E. Sullivan, F. J. Heremans, D. D. Awschalom, S. Guha, and A. M. Dibos, “Nanocavity-mediated Purcell enhancement of Er in TiO₂ thin films grown via atomic layer deposition,” *arXiv* (2023), 10.48550/arxiv.2309.13490, 2309.13490.
- ¹³P. Stevenson, C. M. Phenicie, I. Gray, S. P. Horvath, S. Welinski, A. M. Ferrenti, A. Ferrier, P. Goldner, S. Das, R. Ramesh, R. J. Cava, N. P. d. Leon, and J. D. Thompson, “Erbium-implanted materials for quantum communication applications,” *Phys. Rev. B* **105**, 224106 (2022), 2110.04876.
- ¹⁴T. Xie, J. Rochman, J. G. Bartholomew, A. Ruskuc, J. M. Kindem, I. Craiciu, C. W. Thiel, R. L. Cone, and A. Faraon, “Characterization of e for microwave to optical transduction,” *Physical Review B* **104**, 054111 (2021).
- ¹⁵C. M. Phenicie, P. Stevenson, S. Welinski, B. C. Rose, A. T. Asfaw, R. J. Cava, S. A. Lyon, N. P. d. Leon, and J. D. Thompson, “Narrow Optical Line Widths in Erbium Implanted in TiO₂,” *Nano Lett.* **19**, 8928–8933 (2019), 1909.06304.
- ¹⁶K. Shin, I. Gray, G. Marcaud, S. P. Horvath, F. J. Walker, J. D. Thompson, and C. H. Ahn, “Er-doped anatase TiO₂ thin films on LaAlO₃ (001) for quantum interconnects (QuICs),” *Appl. Phys. Lett.* **121**, 081902 (2022).
- ¹⁷M. K. Singh, G. Wolfowicz, J. Wen, S. E. Sullivan, A. Prakash, A. M. Dibos, D. D. Awschalom, F. J. Heremans, and S. Guha, “Development of a Scalable Quantum Memory Platform – Materials Science of Erbium-Doped TiO₂ Thin Films on Silicon,” *arXiv* (2022), 10.48550/arxiv.2202.05376, 2202.05376.
- ¹⁸B. Jalan, R. Engel-Herbert, J. Cagnon, and S. Stemmer, “Growth modes in metal-organic molecular beam epitaxy of TiO₂ on *r*-plane sapphire,” *Journal of Vacuum Science & Technology A: Vacuum, Surfaces, and Films* **27**, 230–233 (2009).
- ¹⁹A. L. Ankudinov, B. Ravel, J. J. Rehr, and S. D. Conradson, “Real-space multiple-scattering calculation and interpretation of x-ray-absorption near-edge structure,” *Physical Review B* **58**, 7565–7576 (1998).
- ²⁰R. Engel-Herbert, B. Jalan, J. Cagnon, and S. Stemmer, “Microstructure of epitaxial rutile TiO₂ films grown by molecular beam epitaxy on *r*-plane Al₂O₃,” *J. Cryst. Growth* **312**, 149–153 (2009).
- ²¹J. Y. Huang, B. H. Park, D. Jan, X. Q. Pan, Y. T. Zhuk, and Q. X. Jia, “High-resolution transmission electron microscopy study of defects and interfaces in epitaxial TiO₂ films on sapphire and LaAlO₃,” *Philosophical Magazine A* **82**, 735–749 (2002).
- ²²A. M. Stoneham, “Shapes of Inhomogeneously Broadened Resonance Lines in Solids,” *Reviews of Modern Physics* **41**, 82–108 (1969).
- ²³S. Obregón, A. Kubacka, M. Fernández-García, and G. Colón, “High-performance Er³⁺-TiO₂ system: Dual up-conversion and electronic role of the lanthanide,” *Journal of Catalysis* **299**, 298–306 (2013).

TABLE III: Structural parameters from Er and Ti XAFS fitting analysis. The amplitude reduction factor (S_0^2) of 0.93 was determined from Ti K-edge fits and fixed in Er L_3 -edge fits. FEFF simulations used nominal TiO₂ bond lengths. The footnote values correspond to the nominal Ti–O and Ti–Ti bond lengths. Lattice distortions were accounted for during fitting, reflecting observed disorder in higher-R shells. Coordination numbers for higher-R shells (i.e., Ti–Ti₍₂₎ and Er–Ti₍₁₎) are absent due to significant disorder and weak scattering amplitudes.

Probed Atom	Bond	Bond Length (Å)		Debye Waller Factor (Å ²)		Coordination Number	
		0 ppm	500 ppm	0 ppm	500 ppm	0 ppm	500 ppm
Ti K-edge	Ti–O ₍₁₎	1.934 (5) ^a	1.92 (1)	0.0055 (5)	0.0060 (1)	4.1 (2)	4.1 (2)
	Ti–O ₍₂₎	1.978 (5) ^b	1.96 (1)	0.0055 (5)	0.0060 (1)	2.1 (1)	2.1 (1)
	Ti–Ti ₍₁₎	3.02 (1) ^c	3.00 (3)	0.0040 (1)	0.0030 (1)	2 ^d	2 ^d
	Ti–Ti ₍₂₎	3.61 (1) ^e	3.62 (2)	0.0062 (9)	0.0010 (4)	8 ^d	8 ^d
Er L_3 -edge	Er–O ₍₁₎	-	2.20 (1)	-	0.0056 (7)	-	4.3 (2)
	Er–O ₍₂₎	-	2.25 (1)	-	0.0056 (7)	-	2.1 (1)
	Er–Ti ₍₁₎	-	3.09 (3)	-	0.0140 (5)	-	2 ^d

^a 1.944 Å

^b 1.988 Å

^c 2.959 Å

^d Fixed

^e 3.57 Å

- ²⁴J. B. Pérez, M. Courel, R. C. Valderrama, I. Hernández, M. Pal, F. P. Delgado, and N. Mathews, “Structural, optical, and photoluminescence properties of erbium doped TiO₂ films,” *Vacuum* **169**, 108873 (2019).
- ²⁵L. Minervini, M. O. Zacate, and R. W. Grimes, “Defect cluster formation in M₂O₃-doped CeO₂,” *Solid State Ionics* **116**, 339–349 (1999).
- ²⁶G. D. Grant, J. Zhang, I. Masiulionis, S. Chattaraj, K. E. Sautter, S. E. Sullivan, R. Chebrolu, Y. Liu, J. B. Martins, J. Niklas, A. M. Dibos, S. Kewalramani, J. W. Freeland, J. Wen, O. G. Poluektov, F. J. Heremans, D. D. Awschalom, and S. Guha, “Optical and microstructural characterization of Er³⁺ doped epitaxial cerium oxide on silicon,” *APL Materials* **12**, 021121 (2024).
- ²⁷D. T. Cromer and K. Herrington, “The Structures of Anatase and Rutile,” *Journal of the American Chemical Society* **77**, 4708–4709 (1955).
- ²⁸R. Ruus, A. Kikas, A. Saar, A. Ausmees, E. Nõmmiste, J. Aarik, A. Aidla, T. Uustare, and I. Martinson, “Ti 2p and O 1s X-ray absorption of TiO₂ polymorphs,” *Solid State Communications* **104**, 199–203 (1997).
- ²⁹Y. Harada, T. Kinugasa, R. Eguchi, M. Matsubara, A. Kotani, M. Watanabe, A. Yagishita, and S. Shin, “Polarization dependence of soft-x-ray Raman scattering at the L edge of TiO₂,” *Physical Review B* **61**, 12854–12859 (2000).
- ³⁰B. Jiang, J. M. Zuo, N. Jiang, M. O’Keeffe, and J. C. H. Spence, “Charge density and chemical bonding in rutile TiO₂,” *Acta Crystallographica Section A* **59**, 341–350 (2003).
- ³¹P.-H. Hsieh, Y.-M. Lu, W.-S. Hwang, W.-L. Jang, C.-L. Dong, and T.-S. Chan, “X-ray absorption spectroscopy study of thermally annealed Cu–Al–O thin films,” *Materials Chemistry and Physics* **144**, 547–552 (2014).
- ³²G. C. Vásquez, S. Z. Karazhanov, D. Maestre, A. Cremades, J. Piqueras, and S. E. Foss, “Oxygen vacancy related distortions in rutile TiO₂ nanoparticles: A combined experimental and theoretical study,” *Phys. Rev. B* **94**, 235209 (2016).
- ³³F. D. Angelis, C. D. Valentin, S. Fantacci, A. Vittadini, and A. Selloni, “Theoretical Studies on Anatase and Less Common TiO₂ Phases: Bulk, Surfaces, and Nanomaterials,” *Chemical Reviews* **114**, 9708–9753 (2014).
- ³⁴E. G. Seebauer and M. C. Kratzer, “Charged point defects in semiconductors,” *Materials Science and Engineering: R: Reports* **55**, 57–149 (2006).
- ³⁵F. M. F. de Groot, J. C. Fuggle, B. T. Thole, and G. A. Sawatzky, “ $L_{2,3}$ x-ray-absorption edges of d^0 compounds: K⁺, Ca²⁺, Sc³⁺, and Ti⁴⁺ in O_h (octahedral) symmetry,” *Physical Review B* **41**, 928–937 (1990).
- ³⁶P. Krüger, “Multichannel multiple scattering calculation of $L_{2,3}$ -edge spectra of TiO₂ and SrTiO₃: Importance of multiplet coupling and band structure,” *Physical Review B* **81**, 125121 (2010).
- ³⁷W. Li, A. I. Frenkel, J. C. Woicik, C. Ni, and S. I. Shah, “Dopant location identification in Nd³⁺-doped TiO₂ nanoparticles,” *Physical Review B* **72**, 155315 (2005).
- ³⁸G. C. Vásquez, D. Maestre, A. Cremades, J. Ramírez-Castellanos, E. Maggano, S. Nappini, and S. Z. Karazhanov, “Understanding the effects of Cr doping in rutile TiO₂ by DFT calculations and X-ray spectroscopy,” *Sci. Rep.* **8**, 8740 (2018).
- ³⁹B. T. Thole, G. v. d. Laan, J. C. Fuggle, G. A. Sawatzky, R. C. Karnatak, and J.-M. Esteve, “3d x-ray-absorption lines and the $3d^9 4f^{n+1}$ multiplets of the lanthanides,” *Phys. Rev. B* **32**, 5107–5118 (1985).
- ⁴⁰R. Shannon and C. Prewitt, “Effective ionic radii in oxides and fluorides,” *Acta Crystallographica Section B: Structural Crystallography and Crystal Chemistry* **25**, 925–946 (1969).
- ⁴¹W. Luo, C. Fu, R. Li, Y. Liu, H. Zhu, and X. Chen, “Er³⁺-Doped Anatase TiO₂ Nanocrystals: Crystal-Field Levels, Excited-State Dynamics, Upconversion, and Defect Luminescence,” *Small* **7**, 3046–3056 (2011).
- ⁴²Z. Rao, X. Xie, X. Wang, A. Mahmood, S. Tong, M. Ge, and J. Sun, “Defect Chemistry of Er³⁺-Doped TiO₂ and Its Photocatalytic Activity for the Degradation of Flowing Gas-Phase VOCs,” *The Journal of Physical Chemistry C* **123**, 12321–12334 (2019).